


THE STELLAR AND DARK MATTER DISTRIBUTIONS IN ELLIPTICAL GALAXIES MEASURED BY STACKED WEAK GRAVITATIONAL LENSING

MOMOKA FUJIKAWA¹ AND MASAMUNE OGURI^{1,2} 

¹Department of Physics, Graduate School of Science, Chiba University, 1-33 Yayoi-Cho, Inage-Ku, Chiba 263-8522, Japan and

²Center for Frontier Science, Chiba University, 1-33 Yayoi-cho, Inage-ku, Chiba 263-8522, Japan

Version December 11, 2025

Abstract

We investigate stellar mass and central dark matter density profiles of photometric luminous red galaxies with stellar masses of $\sim 10^{10} - 10^{12} M_{\odot}$ using weak gravitational lensing measurements from the Hyper Suprime-Cam Subaru Strategic Program data obtained with the Subaru Telescope. By stacking weak lensing signals from a large number of galaxies, we obtain average tangential shear profiles down to $\sim 10 \text{ kpc}/h$, which are fitted assuming a two-component model consisting of stellar and dark matter components to constrain their central dark matter distribution. We find a preference for non-zero core radii of dark matter distributions in galaxies with stellar masses of $\sim 10^{11} M_{\odot}$. Our results imply a stronger feedback effect than that typically predicted by current hydrodynamical simulations. In addition, we provide a new constraint on the stellar-to-halo mass relation, where both stellar and halo masses are, for the first time, directly constrained by weak gravitational lensing. Our results prefer the stellar initial mass function (IMF) that is more bottom-heavy than the Salpeter IMF.

Subject headings: Dark matter distribution, Elliptical galaxies, Weak gravitational lensing

1. INTRODUCTION

The standard cosmological model is now established through both theoretical and observational approaches. In this standard model, the Cold Dark Matter (CDM) is assumed to be the form of dark matter. The CDM model neglects any interactions other than gravity in structure formation and assumes that the free streaming is ineffective. The free streaming refers to the suppression of density fluctuations caused by the free motion of dark matter particles with the large velocity dispersion. Since CDM does not experience such suppression, it allows the formation of structures down to very small scales.

While the standard cosmological model successfully explains large scale observations, it shows contradictions to some of smaller scale observations, such as those of dwarf galaxies. This is known as the small-scale challenges (Bullock & Boylan-Kolchin 2017). One of these small-scale challenges is the core-cusp problem, which refers to the discrepancy between the central density profiles of dark matter halos predicted by CDM simulations and those measured from observations. The density distribution of a CDM halo is known to follow the Navarro-Frenk-White (NFW) profile (Navarro et al. 1997),

$$\rho(r) = \frac{\rho_s}{\left(1 + \frac{r}{r_s}\right)^2}, \quad (1)$$

where r is the distance from the halo center, ρ is the mass density, ρ_s is the characteristic density, and r_s is the scale radius. In the inner region of the halo, where $r \ll r_s$, the density behaves as $\rho(r) \propto r^{-1}$, indicating a cuspy profile. In contrast, several observational studies report cored dark matter distributions with nearly constant central

densities (e.g., Oh et al. 2015).

To address these small-scale challenges, various studies have been conducted at various mass scales. Among others, the central structure of elliptical galaxies has been studied mainly using strong gravitational lensing and stellar dynamics, from which it has been shown that the total density profile follows an approximately isothermal form, $\rho(r) \propto r^{-2}$ (e.g., Koopmans et al. 2006; Gavazzi et al. 2007; Barnabè et al. 2011; Bolton et al. 2012; Cappellari et al. 2013; Sonnenfeld et al. 2013; Li et al. 2018; Etherington et al. 2023). Separating stellar and dark matter distributions requires breaking the degeneracy between the stellar initial mass function (IMF) and the dark matter fraction, which have been attempted using strong gravitational lensing (e.g., Rusin et al. 2003; Treu et al. 2010; Auger et al. 2010; Grillo 2012; Oguri et al. 2014; Sonnenfeld et al. 2019; Sonnenfeld 2025), stellar dynamics (e.g., Cappellari et al. 2012; Cappellari 2016; Alabi et al. 2017; Santucci et al. 2022; Ding et al. 2023; Zhu et al. 2024; Yang et al. 2024), combining strong lensing and stellar dynamics (e.g., Treu & Koopmans 2004; Sonnenfeld et al. 2015; Newman et al. 2015; Oldham & Auger 2018; Shajib et al. 2021; Sheu et al. 2025), and combining strong and weak lensing (e.g., Gavazzi et al. 2007; Sonnenfeld et al. 2018).

Recently, on the other hand, advances in observational techniques have made it possible to probe the inner density profiles of galaxies even through weak gravitational lensing. For instance, the possibility of probing the inner density profile of dwarf galaxies with stacked weak lensing is considered in Kobayashi et al. (2015). Khadka et al. (2024) used stacked weak lensing at $> 0.1 \text{ Mpc}$ to break the mass-sheet degeneracy inherent to the strong lensing analysis.

In this study, we conduct the first systematic analysis

of the stellar mass and dark matter distributions in centers of elliptical galaxies using stacked weak gravitational lensing. Since weak lensing probes the relatively outer regions of galaxy centers compared to methods using the velocity dispersion or strong lensing, our approach provides a means of studying central density profiles that is complementary to previous approaches. For this purpose, we employ the Hyper Suprime-Cam Subaru Strategic Program (HSC-SSP; Aihara et al. 2018) data that achieve both the wide area and the high number density of galaxies used for weak lensing.

This paper is organized as follows. In Section 2, we describe the HSC-SSP data used for our analysis as well as models to fit the data. We show our results in Section 3. We give our conclusion in Section 4. Throughout the paper we assume a flat Universe with the matter density $\Omega_m = 0.3$, the cosmological constant $\Omega_\Lambda = 0.7$, the baryon matter density $\Omega_b = 0.05$, the normalization of the matter power spectrum $\sigma_8 = 0.81$, the spectral index $n_s = 0.96$, and the dimensionless Hubble constant $h = 0.7$.

2. DATA AND MODEL

2.1. Subaru HSC-SSP

We use the HSC-SSP three-year shear catalog (Li et al. 2022) for our weak lensing analysis. This catalog covers an area of $\sim 430 \text{ deg}^2$ with the raw galaxy number density of $\sim 23 \text{ arcmin}^{-2}$, and is validated with a series of null tests for systematics.

For a foreground lens sample, we employ the HSC-SSP final-year photometric luminous red galaxy (LRG) sample (Oguri et al. 2025). The photometric LRG sample is constructed based on the stellar population synthesis fitting of individual galaxies with the model of quiescent elliptical galaxies based on Bruzual & Charlot (2003), which is also used for the CAMIRA cluster finding algorithm (Oguri 2014; Oguri et al. 2018a,b). The final-year photometric LRG sample covers an area of $\sim 1200 \text{ deg}^2$ and contains galaxies in the photometric redshift range of $0.05 \leq z_{\text{LRG}} \leq 1.25$ and the stellar mass range of $M_\star \geq 10^{10.3} M_\odot$, where the stellar mass is derived assuming the Salpeter (1955) IMF. As shown in Oguri et al. (2025), their photometric redshifts are accurate and precise at $\sigma_z \lesssim 0.02$ in the redshift range of $0.4 \lesssim z_{\text{LRG}} \lesssim 1$.

We measure the differential surface density profile $\Delta\Sigma(r)$ around a sample of photometric LRGs with the standard approach described in detail in e.g., Mandelbaum et al. (2018) and Medezinski et al. (2018). Specifically, for each radial bin centered at r , it is estimated as

$$\Delta\Sigma(r) = \frac{1}{2\mathcal{R}} \frac{\sum_{l,s} w_{ls} \langle \Sigma_{\text{cr}}^{-1} \rangle_{ls}^{-1} (e_{+,ls} - 2\mathcal{R}c_{+,ls})}{(1+K) \sum_{l,s} w_{ls}}, \quad (2)$$

where l and s denote the lens and the source, respectively, $e_{+,ls}$ is the tangential shear for each lens and source pair, $c_{+,ls}$ is the additive shear bias of the same tangential shear component, the shear responsivity is

$$\mathcal{R} = 1 - \frac{\sum_{l,s} \sigma_{\text{rms},s}^2 w_{ls}}{\sum_{l,s} w_{ls}}, \quad (3)$$

with $e_{\text{rms},s}$ being the root-mean-square ellipticity for the source s , K is computed from the multiplicative shear

bias m_s as

$$K = \frac{\sum_{l,s} m_s w_{ls}}{\sum_{l,s} w_{ls}}, \quad (4)$$

and the weight factor w_{ls} is

$$w_{ls} = \frac{\langle \Sigma_{\text{cr}}^{-1} \rangle_{ls}^2}{\sigma_{e,s}^2 + \sigma_{\text{rms},s}^2}, \quad (5)$$

where $\sigma_{e,s}$ is the measurement error of the ellipticity and $\langle \Sigma_{\text{cr}}^{-1} \rangle_{ls}$ is the average inverse critical surface density computed from the probability distribution function $P(z_s)$ of the photometric redshift of the source s as

$$\langle \Sigma_{\text{cr}}^{-1} \rangle_{ls} = \int_{z_1}^{\infty} dz_s \Sigma_{\text{cr}}^{-1}(z_l, z_s) P(z_s). \quad (6)$$

We adopt DNNz photometric redshifts (A. J. Nishizawa et al., in prep.) for photometric redshifts of source galaxies. The error on $\Delta\Sigma(r)$ is derived from the weighted sum of ellipticity errors of individual source galaxies, $\sigma_{e,s}^2 + \sigma_{\text{rms},s}^2$. Since we are interested in lensing profiles at relatively small radii where the intrinsic shape noise dominates (see e.g., Hoekstra 2003), throughout the paper, we consider the intrinsic shape noise only and ignore the cosmic shear noise.

One of the most important sources of systematic errors, which is relevant particularly at small radii, is the dilution effect by neighboring galaxies. Due to clustering of galaxies, there is a higher probability of having their redshifts almost same as that of a lensing object, which is usually not accounted for in deriving $P(z_s)$ and hence biases lensing measurements. As shown in e.g., Medezinski et al. (2018), this dilution effect can be mitigated by carefully selecting background source galaxies and using only them for the weak lensing analysis. In this paper, we employ the so-called $P(z)$ cut method (Oguri 2014) for which we only use source galaxies that satisfy

$$\int_{z_1+\Delta z}^{\infty} dz_s P(z_s) > P_{\text{cut}}. \quad (7)$$

While we fix $\Delta z = 0.1$ and $P_{\text{cut}} = 0.95$, in Appendix A we explicitly check the robustness of our result with respect to the choice of the value of P_{cut} .

2.2. Model of the inner density profile

For fitting the inner region of the observed differential surface density distribution, we use a two-component model consisting of a stellar matter component and a dark matter component. For the stellar matter component, we adopt the Hernquist density profile (Hernquist 1990)

$$\rho(r) = \frac{M_\star}{2\pi} \frac{a}{r} \frac{1}{(r+a)^3}, \quad (8)$$

where M_\star is the stellar mass. The scale radius a is related to the effective (half-light) radius r_e as

$$r_e \approx 1.8153a. \quad (9)$$

The mass enclosed within a radius r is given by the following equation

$$M_{\star,3D}(< r) = M_\star \frac{r^2}{(r+a)^2}. \quad (10)$$

Analytic expressions of lensing profiles of the Hernquist profile are given in [Keeton \(2001\)](#).

For the dark matter component, we consider a model that has a core at the center and follows a power law in the outer region. We define the three-dimensional density profile as

$$\rho_{\text{DM}}(r) = M_{\star} \frac{3+\gamma}{2\pi^{3/2} r_e^3} \frac{\Gamma(-\frac{\gamma}{2})}{\Gamma(-\frac{1+\gamma}{2})} A \left(\frac{r^2 + r_c^2}{r_e^2} \right)^{\gamma/2}, \quad (11)$$

where $\Gamma(x)$ is the gamma function, γ is the radial slope of the density profile, A is the dimensionless parameter that determines the normalization, and r_c is the core radius. From the definition of the surface mass density, we obtain

$$\Sigma_{\text{DM}}(r) = \int_{-\infty}^{\infty} \rho_{\text{DM}}(\sqrt{r^2 + Z^2}) dZ \quad (12)$$

$$= M_{\star} \frac{3+\gamma}{2\pi r_e^{3+\gamma}} A (r^2 + r_c^2)^{\frac{1+\gamma}{2}}. \quad (13)$$

Furthermore, the two-dimensional enclosed mass can be expressed in terms of the surface mass density as

$$M_{\text{DM},2\text{D}}(< r) = \int_0^r 2\pi r' \Sigma_{\text{DM}}(r') dr' \quad (14)$$

$$= M_{\star} A \left(\frac{r_c}{r_e} \right)^{3+\gamma} \left[\left(1 + \frac{r^2}{r_c^2} \right)^{\frac{3+\gamma}{2}} - 1 \right]. \quad (15)$$

In addition, the average surface mass density within the radius r is given by

$$\bar{\Sigma}_{\text{DM}}(< r) = \frac{M_{\text{DM},2\text{D}}(< r)}{\pi r^2} \quad (16)$$

$$= \frac{M_{\star} A}{\pi r^2} \left(\frac{r_c}{r_e} \right)^{3+\gamma} \left[\left(1 + \frac{r^2}{r_c^2} \right)^{\frac{3+\gamma}{2}} - 1 \right]. \quad (17)$$

From these results, the differential surface mass density is computed as

$$\Delta\Sigma_{\text{DM}}(r) = \bar{\Sigma}_{\text{DM}}(< r) - \Sigma_{\text{DM}}(r) \quad (18)$$

$$= \frac{M_{\star} A}{\pi r_e^{3+\gamma}} \left\{ \frac{1}{r^2} \left[(r^2 + r_c^2)^{\frac{3+\gamma}{2}} - r_c^{3+\gamma} \right] - \frac{3+\gamma}{2} (r^2 + r_c^2)^{\frac{1+\gamma}{2}} \right\}. \quad (19)$$

An advantage of this cored power-law profile is that the lensing profiles can be calculated analytically. While this model is rather simplistic, we expect that the relatively narrow fitting range of inner lensing profiles in our analysis as described in Section 2.4 justifies the use of this simple analytic profile.

We fit the sum of the two components

$$\Delta\Sigma(r) = \Delta\Sigma_{\star}(r) + \Delta\Sigma_{\text{DM}}(r), \quad (20)$$

to the observational data.

2.3. Model of the outer density profile

While our main focus is the inner density profile, we also fit the outer lensing profile to estimate the halo mass and compare our analysis result of the inner density profile with an extrapolation of the NFW profile fitted to the outer lensing profile. Here a complication lies in the fact that all the photometric LRGs are not necessarily central galaxies within halos, but can correspond to satellite galaxies in the outer part of massive halos. We thus fit the outer lensing profile to the following simple model

$$\Delta\Sigma(r) = \Delta\Sigma_{\text{cen}}(r; M) + f_{\text{sat}} \Delta\Sigma_{\text{sat}}(r; M_{\text{h}}) + \Delta\Sigma_{2\text{h}}(r; M, M_{\text{h}}), \quad (21)$$

for which we assume that photometric LRGs are hosted by halos with the average mass M and the fraction f_{sat} of photometric LRGs corresponds to satellite galaxies with the average host mass M_{h} . Following the analysis of ray-tracing simulations presented in [Oguri & Hamana \(2011\)](#), we model $\Delta\Sigma_{\text{cen}}(r; M)$ by a smoothly truncated NFW density profile ([Baltz et al. 2009](#)) with the truncation radius $r_t/r_{\text{vir}} = 2.5$. We model the satellite component as

$$\Delta\Sigma_{\text{sat}}(r; M_{\text{h}}) = \int \frac{k dk}{2\pi} \frac{\left\{ \tilde{\Sigma}(k; M_{\text{h}}) \right\}^2}{M_{\text{h}}} J_2(kr), \quad (22)$$

where $\tilde{\Sigma}$ is the Fourier transform of the [Baltz et al. \(2009\)](#) density profile and $J_2(x)$ is the Bessel function of order 2. For both $\Delta\Sigma_{\text{cen}}(r; M)$ and $\Delta\Sigma_{\text{sat}}(r; M_{\text{h}})$, we adopt the mass-concentration relation of [Diemer & Kravtsov \(2015\)](#) and [Diemer & Joyce \(2019\)](#) implemented in the `colossus` package ([Diemer 2018](#)). We compute the 2-halo term as

$$\Delta\Sigma_{2\text{h}}(r; M, M_{\text{h}}) = \int \frac{k dk}{2\pi} \bar{\rho}_{\text{m}0} \bar{b} P_{\text{m}}(k/(1+z); z) J_2(kr), \quad (23)$$

where $\bar{\rho}_{\text{m}0}$ is the average matter density of the Universe at $z = 0$, $P_{\text{m}}(k/(1+z); z)$ is the linear matter power spectrum, and the average halo bias \bar{b} is

$$\bar{b} = (1 - f_{\text{sat}}) b(M) + f_{\text{sat}} b(M_{\text{h}}), \quad (24)$$

with $b(M)$ being computed by the model of [Tinker et al. \(2010\)](#).

2.4. Fitting method

For the lensing profile fittings, we perform a chi-square analysis using χ^2 defined by

$$\chi^2 = \sum_{i=1}^N \frac{[\Delta\Sigma_{\text{obs},i} - f_{\text{model}}(r_i)]^2}{\sigma_i^2}, \quad (25)$$

$$f_{\text{model}}(r) = \frac{\Delta\Sigma(r)}{1 - \langle \Sigma_{\text{cr}}^{-1} \rangle \Sigma(r)}. \quad (26)$$

Here, $\Delta\Sigma_{\text{obs}}$ and σ are the differential surface mass density and its error obtained from the weak lensing measurement, respectively, i labels the radial bin, and $\Delta\Sigma$ and Σ are the model predictions based on the inner or outer density profile mentioned above. In computing $f_{\text{model}}(r)$, we include the correction of the surface mass density profile to take account of the fact that observed

$\log_{10}(M_{\star,\text{in}}[M_{\odot}])$	N_{LRG}	r_e [Mpc/h]	A	γ	r_c [Mpc/h]	$M_{\star,\text{fit}} [M_{\odot}/h]$	$\chi^2_{\text{in}}/\text{dof}$
10.3–10.5	1.81×10^5	1.4×10^{-3}	$7.5^{+12.0}_{-6.0}$	$-2.50^{+0.50}_{-0.00}$	$1.8^{+0.4}_{-0.9} \times 10^{-2}$	$3.0^{+1.5}_{-2.2} \times 10^{10}$	9.4/5
10.5–10.7	2.05×10^5	1.4×10^{-3}	$0.2^{+4.0}_{-0.0}$	$-1.51^{+0.06}_{-0.29}$	$0.0^{+1.5}_{-0.0} \times 10^{-2}$	$2.5^{+4.1}_{-2.3} \times 10^{10}$	10.2/5
10.7–10.9	2.23×10^5	1.4×10^{-3}	$2.7^{+0.4}_{-2.1}$	$-2.50^{+0.33}_{-0.00}$	$1.7^{+0.3}_{-0.4} \times 10^{-2}$	$9.0^{+1.5}_{-1.5} \times 10^{10}$	11.8/5
10.9–11.1	2.08×10^5	1.5×10^{-3}	$1.9^{+0.3}_{-1.6}$	$-2.50^{+0.41}_{-0.00}$	$2.4^{+0.5}_{-0.6} \times 10^{-2}$	$1.7^{+0.2}_{-0.1} \times 10^{11}$	8.8/5
11.1–11.3	1.49×10^5	1.8×10^{-3}	$1.9^{+0.7}_{-1.8}$	$-2.46^{+0.76}_{-0.04}$	$2.5^{+0.5}_{-1.3} \times 10^{-2}$	$2.2^{+0.1}_{-0.2} \times 10^{11}$	19.2/5
11.3–11.5	5.54×10^4	2.3×10^{-3}	$0.2^{+3.9}_{-0.1}$	$-1.83^{+0.52}_{-0.67}$	$1.8^{+1.7}_{-1.8} \times 10^{-2}$	$2.7^{+0.4}_{-1.3} \times 10^{11}$	11.1/5
11.5–11.7	1.02×10^4	3.3×10^{-3}	$0.2^{+8.0}_{-0.1}$	$-1.56^{+0.55}_{-0.52}$	$1^{+16}_{-1} \times 10^{-3}$	$2.7^{+1.6}_{-2.5} \times 10^{11}$	6.4/5

TABLE 1

PARAMETERS USED IN THE INNER PROFILE FITTING. N_{LRG} DENOTES THE NUMBER OF LRGs USED AS LENS GALAXIES, AND r_e REPRESENTS THE HALF-LIGHT RADIUS. THE ERRORS ARE SHOWN AT THE 1σ LEVEL.

lensing shear profiles are reduced shear. The errors on the parameters are estimated from the distribution of

$$\Delta\chi^2(x) = \chi^2_{\text{min}}(x) - \chi^2_{\text{min}}, \quad (27)$$

where $\chi^2_{\text{min}}(x)$ is the minimum χ^2 value when a parameter x is fixed, and χ^2_{min} is the minimum χ^2 value when all parameters are allowed to vary.

We divide the stellar mass of LRGs into seven bins in the range $10^{10.3}M_{\odot} < M_{\star} < 10^{11.7}M_{\odot}$, and measure the lensing profile for each bin. We restrict our analysis to the lens redshift range of $0.4 < z < 0.6$. This choice of the redshift range is motivated by several reasons, including the fact that the lensing signal is strongest in this redshift range given the depth of the HSC-SSP, the photometric redshift accuracy of photometric LRGs is best, and at lower redshifts, high surface brightnesses of lensing galaxies can obscure background galaxies or bias their shape measurements near centers of lensing galaxies.

For the inner lensing profile fitting, we treat $M_{\star,\text{fit}}$, A , γ , and r_c as parameters. Here, the stellar mass $M_{\star,\text{fit}}$ is treated as a free parameter independently of observed stellar masses of photometric LRGs, which we denote $M_{\star,\text{in}}$ hereafter, because the true stellar mass can significantly differ from $M_{\star,\text{in}}$ considering various effects such as the uncertainty of the stellar IMF, systematic errors in inferring stellar masses with the stellar population synthesis fitting, and systematic errors in measuring total magnitudes of bright galaxies in the HSC-SSP data (Huang et al. 2018). We calculate the effective radius r_e for each $M_{\star,\text{in}}$ bin based on Abe et al. (2025), which adopts the model of van der Wel et al. (2024), and ignore its uncertainty because our fitting range of radii (see below) is typically much larger than r_e and hence its uncertainty does not significantly affect our result. The values of r_e are summarized in Table 1. We exclude the very central region from the fitting range because the weak lensing signal in that range suffers from large statistical and systematic errors (see Appendix A.1). The fitting is therefore performed within the range $0.013 \text{ Mpc}/h < r < 0.1 \text{ Mpc}/h$. In addition, since values of the core radius r_c larger than this fitting range are not physically meaningful, we set its upper limit to $0.1 \text{ Mpc}/h$. We note that observed reduced shear values in this fitting range are $g \lesssim 0.1$, which is well within the range where current shape measurement techniques can accurately measure weak lensing shear (e.g., Okabe & Smith 2016; Hernández-Martín et al. 2020).

For the outer lensing profile fitting, we treat M , M_h ,

and f_{sat} as parameters. The fitting range is set from $r = 0.04 \text{ Mpc}/h$, where the $\Delta\Sigma_{\text{cen}}$ component begins to dominate, to $r = 3 \text{ Mpc}/h$, where the effect of cosmic shear on the statistical error of the tangential shear measurement can be considered negligible. Also, we set the upper limit of f_{sat} to 0.4 given the constraint on f_{sat} from the halo-model analysis of the clustering of photometric LRGs (Ishikawa et al. 2021).

3. RESULT

3.1. Inner profile fitting

In Figure 1, we show the differential surface density profiles obtained from the weak lensing measurements, along with the results of fitting the inner mass density profile using the model described in Equation (20), for all stellar mass bins. We find that in the central region, the stellar mass component dominates, while in the outer region, the dark matter component becomes predominant. The sum of the stellar mass and dark matter components reproduces the observed differential surface density profiles well. The best-fit parameters for each stellar mass bin are summarized in Table 1. For the stellar mass bin $10^{11.1}M_{\odot} < M_{\star,\text{in}} < 10^{11.3}M_{\odot}$, the best-fit χ^2 value falls outside the 95% confidence interval ($0.8 \lesssim \chi^2 \lesssim 12.8$), indicating that the results for this bin should be interpreted with caution.¹ The result for the stellar mass bin $10^{11.3}M_{\odot} < M_{\star,\text{in}} < 10^{11.5}M_{\odot}$ should also be interpreted with caution, because the effect of the photometric redshift uncertainty of LRGs may not be negligible for this stellar mass bin (see Appendix A.2).

We compare the best-fit stellar masses with those measured from the HSC-SSP photometric data. As shown in Figure 2, the best-fit stellar masses tend to be larger than the HSC estimates, and in some stellar mass bins, the differences are significantly larger than the statistical errors. However, as noted above, the difference can be explained by the mixture of systematic errors in measurements of stellar masses in the HSC-SSP data and the uncertainty of the stellar IMF. The fact that best-fit stellar masses with weak lensing exhibit a clear positive correlation with the HSC-SSP measurements can support the validity of our lensing analysis.

Furthermore, we find a negative correlation between the radial slope of the dark matter density profile γ and the core radius r_c , as shown in Figure 3. This can be naturally explained by the fact that increasing the core

¹ We note that, since we examine 35 independent χ^2 including those presented in Appendix, a few χ^2 values can fall outside the 95% confidence interval simply by statistical flukes.

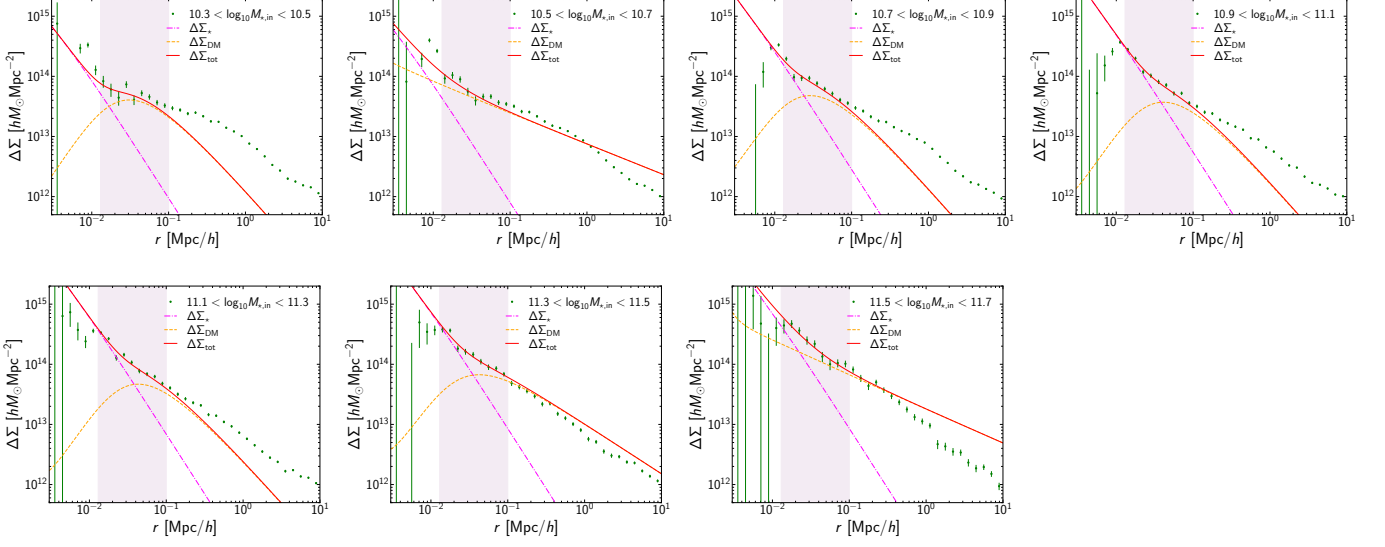


FIG. 1.— Surface mass density profiles $\Delta\Sigma$ obtained from weak lensing measurements and the results of fitting the inner profiles. Different panels show results for different stellar mass bins. The green points show the observational results from stacked weak gravitational lensing. The magenta dash-dotted, the orange dashed, and the red solid lines indicate the stellar matter component, the dark matter component, and the total mass, respectively. The shaded region denotes the fitting range.

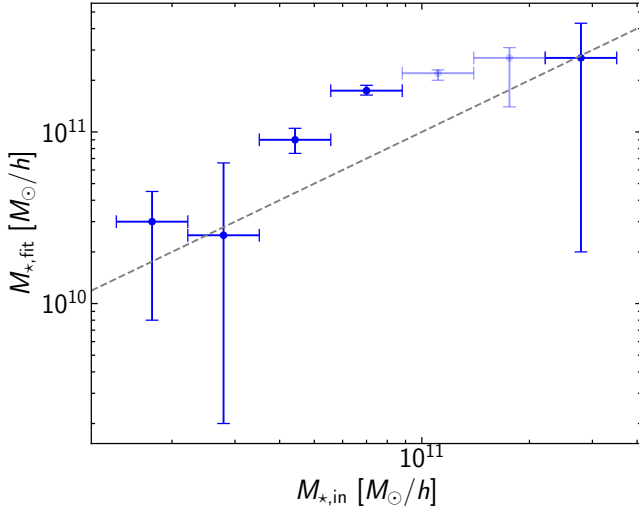


FIG. 2.— Comparison of best-fit stellar masses $M_{\star,\text{fit}}$ with those measured from the HSC-SSP photometric data, $M_{\star,\text{in}}$. The blue points show our results and the dashed line shows $M_{\star,\text{fit}} = M_{\star,\text{in}}$. Points shown by the lighter color might be affected by systematic errors and therefore should be interpreted with caution (see the text for more details).

radius reduces the dark matter density in the central region, which is compensated by an increase in the stellar mass. As the stellar matter component becomes more dominant, the dark matter density profile steepens, and the value of γ decreases. Also, while core radii of dark matter distributions are consistent with zero within 2σ for most stellar mass bins, two bins with $10^{10.7}M_{\odot} < M_{\star,\text{in}} < 10^{10.9}M_{\odot}$ and $10^{10.9}M_{\odot} < M_{\star,\text{in}} < 10^{11.1}M_{\odot}$ show core radii that remain inconsistent with zero even within 3σ , suggesting that cored dark matter density profiles are observed for these galaxies.

3.2. Comparison with the NFW profile

We compare the dark matter density profile obtained from the inner profile fitting with the NFW profile. For

this purpose, the outer lensing profile is fitted with an NFW-based model given by Equation (21) to determine the mass of the central NFW component. The best-fit parameters for each stellar mass bin are summarized in Table 2. The resulting NFW profile is then extrapolated inward and compared with the dark matter distribution obtained from the inner profile fitting. The results of the outer profile fitting are shown in Figure 4.

For a more quantitative comparison, we evaluate their differences with the ratio of the two profiles. Specifically, we define

$$f_{\Sigma}(r) = \frac{\Sigma_{\text{DM}}(r)}{\Sigma_{\text{NFW}}(r)}, \quad (28)$$

as the ratio of the surface mass densities and

$$f_{\Delta\Sigma}(r) = \frac{\Delta\Sigma_{\text{DM}}(r)}{\Delta\Sigma_{\text{NFW}}(r)}, \quad (29)$$

as the ratio of the differential surface mass densities. We show $f_{\Sigma}(r)$ and $f_{\Delta\Sigma}(r)$ in Figures 5 and 6, respectively. In the two stellar mass bins where cored dark matter distributions are identified, both $f_{\Sigma}(r)$ and $f_{\Delta\Sigma}(r)$ fall below 1 in the central region, and are inconsistent with 1 at more than 3σ level. This result supports the interpretation that the central dark matter profiles in these two stellar mass bins deviate from the NFW form. For the other stellar mass bins, $f_{\Sigma}(r)$ and $f_{\Delta\Sigma}(r)$ are consistent with 1 within $\sim 2\sigma$, indicating that the central dark matter profiles agree well with the NFW profile. In contrast, our result appears to disfavor the enhancement of central dark matter profiles due to the adiabatic contraction (e.g., Gnedin et al. 2004).

3.3. Dark matter fractions

The formation of the core for the intermediate stellar mass bins, where the stellar mass fractions to the total halo masses are large, can be attributed to the baryonic feedback. To quantitatively investigate this effect, we

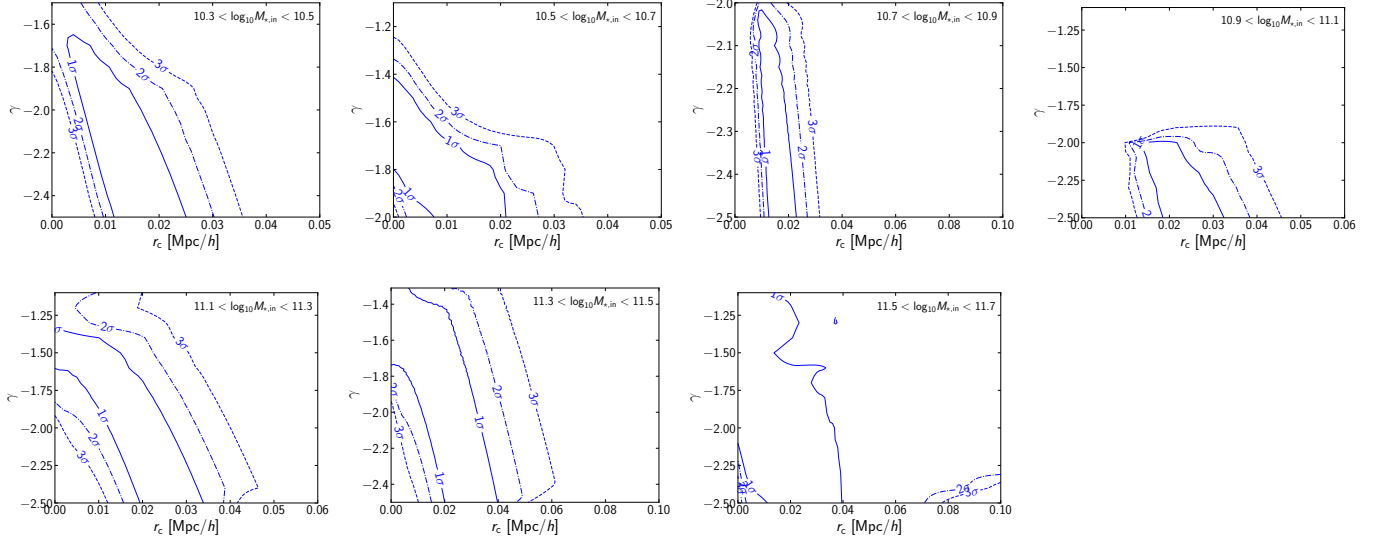


FIG. 3.— The projected constraint on parameters from the inner profile fitting in the γ - r_c plane. Different panels show results for different stellar mass bins.

$\log_{10}(M_{*,in}[M_{\odot}])$	$M_{\text{NFW}} [M_{\odot}/h]$	$M_h [M_{\odot}/h]$	f_{sat}	$\chi^2_{\text{out}}/\text{dof}$
10.3–10.5	$1.2^{+0.1}_{-0.1} \times 10^{12}$	$5.1^{+0.1}_{-0.1} \times 10^{13}$	$0.40^{+0.00}_{-0.01}$	19.3/16
10.5–10.7	$1.3^{+0.1}_{-0.1} \times 10^{12}$	$5.4^{+0.5}_{-0.4} \times 10^{13}$	$0.32^{+0.02}_{-0.02}$	20.9/16
10.7–10.9	$1.4^{+0.1}_{-0.1} \times 10^{12}$	$5.5^{+0.6}_{-0.1} \times 10^{13}$	$0.27^{+0.02}_{-0.02}$	19.3/16
10.9–11.1	$1.8^{+0.1}_{-0.1} \times 10^{12}$	$6.8^{+0.9}_{-0.7} \times 10^{13}$	$0.21^{+0.02}_{-0.02}$	31.4/16
11.1–11.3	$2.6^{+0.2}_{-0.1} \times 10^{12}$	$6.7^{+1.1}_{-0.6} \times 10^{13}$	$0.21^{+0.02}_{-0.03}$	13.31/16
11.3–11.5	$4.7^{+0.4}_{-0.3} \times 10^{12}$	$1.1^{+0.4}_{-0.3} \times 10^{14}$	$0.14^{+0.03}_{-0.03}$	19.2/16
11.5–11.7	$7.6^{+1.3}_{-1.2} \times 10^{12}$	$4.9^{+4.1}_{-1.6} \times 10^{13}$	$0.30^{+0.10}_{-0.10}$	16.0/16

TABLE 2
PARAMETERS USED IN THE OUTER PROFILE FITTING. HERE, M_{NFW} CORRESPONDS TO M IN SECTION 2.3. THE ERRORS ARE SHOWN AT THE 1σ LEVEL.

$\log_{10}(M_{*,in}[M_{\odot}])$	$f_{\text{DM}}(< 5r_e)$
10.3–10.5	$0.19^{+0.70}_{-0.12}$
10.5–10.7	$0.51^{+0.45}_{-0.47}$
10.7–10.9	$0.087^{+0.125}_{-0.050}$
10.9–11.1	$0.035^{+0.050}_{-0.017}$
11.1–11.3	$0.056^{+0.431}_{-0.025}$
11.3–11.5	$0.14^{+0.53}_{-0.08}$
11.5–11.7	$0.50^{+0.42}_{-0.49}$

TABLE 3
THE VALUES OF THE DARK MATTER FRACTIONS $f_{\text{DM}}(< 5r_e)$. THE ERRORS ARE SHOWN AT THE 1σ LEVEL.

examine the dark matter fraction within $5r_e$ defined by

$$f_{\text{DM}}(< 5r_e) = \frac{M_{\text{DM},3D}(< 5r_e)}{M_{*,3D}(< 5r_e) + M_{\text{DM},3D}(< 5r_e)}, \quad (30)$$

which are shown in Table 3 and Figure 7. Similarly to the results from the previous work based on globular cluster kinematics and orbit-based dynamical models (Alabi et al. 2017; Yang et al. 2024), we find that the dark matter fraction in the stellar mass bins where cored central density profiles are observed is lower than the values predicted by the EAGLE (Schaye et al. 2015; Crain et al. 2015) and TNG-100 simulations (Naiman et al.

2018; Marinacci et al. 2018; Pillepich et al. 2018; Nelson et al. 2018; Springel et al. 2018). This result suggests that the actual feedback effect may be stronger than predicted by the simulations. We note that similar results have been obtained from the rotation-curve analysis of late-type galaxies (Hayashi et al. 2025).

3.4. Stellar-to-halo mass relation

In Section 3.1, we constrain the stellar mass from the inner profile fitting, and in Section 3.2, we constrain the NFW halo mass by fitting the outer profile. These results allow us to constrain the Stellar-to-halo mass relation (SHMR). In this approach, unlike the conventional approach that estimates stellar masses from spectral energy density fitting, the SHMR is constrained using only weak gravitational lensing. The result is shown in Figure 8. Compared to the case assuming the Salpeter IMF (Behroozi et al. 2019; Abe et al. 2025), the stellar mass for a given halo-mass tends to be higher. Our result suggests the possibility of the stellar IMF that is more bottom-heavy than the Salpeter IMF. The bottom-heavy stellar IMF in massive elliptical galaxies is qualitatively consistent with previous findings based on spectral absorption lines (e.g., van Dokkum & Conroy 2010), stellar kinematics (e.g., Cappellari et al. 2012), and quasar microlensing (e.g., Oguri et al. 2014; Schechter et al. 2014).

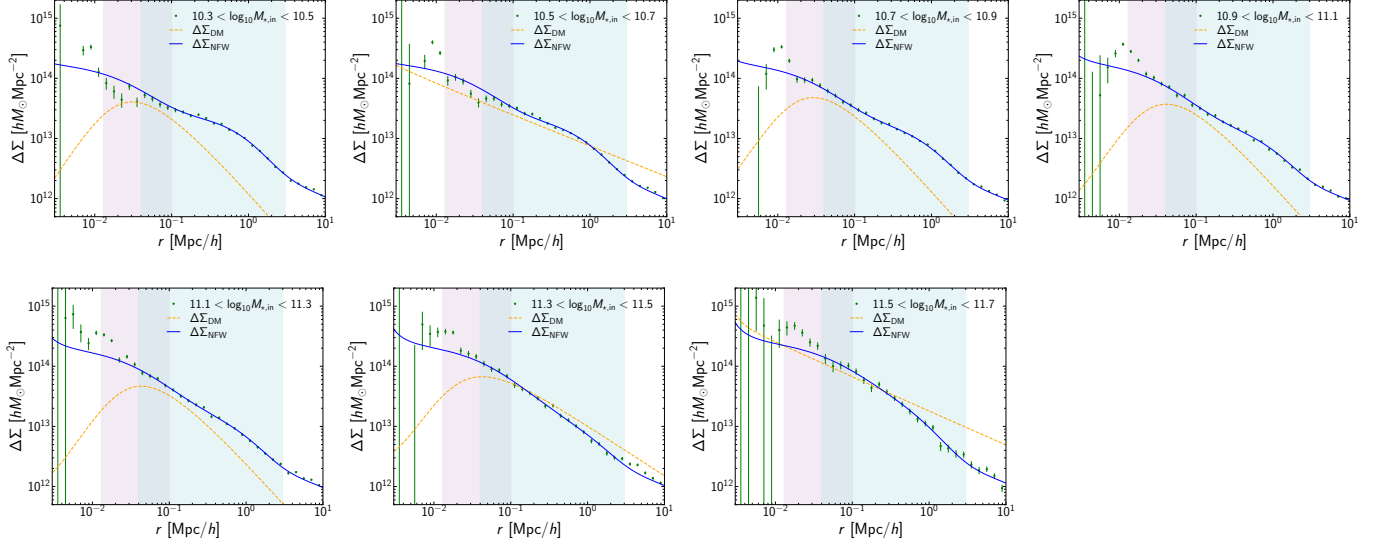


FIG. 4.— Comparison between the dark matter density profile obtained from the inner profile fitting and the NFW profile fitted to the outer lensing profile, where the NFW profile includes additional contributions from the satellite component as well as 2-halo term (see Equation 21). Different panels show results for different stellar mass bins. The orange dashed and blue solid lines indicate the dark matter distribution inferred from inner profile fitting and the NFW profile from the outer profile fitting, respectively. The magenta-shaded region denotes the inner-fitting range, and the light-blue shaded region shows the outer-fitting range.

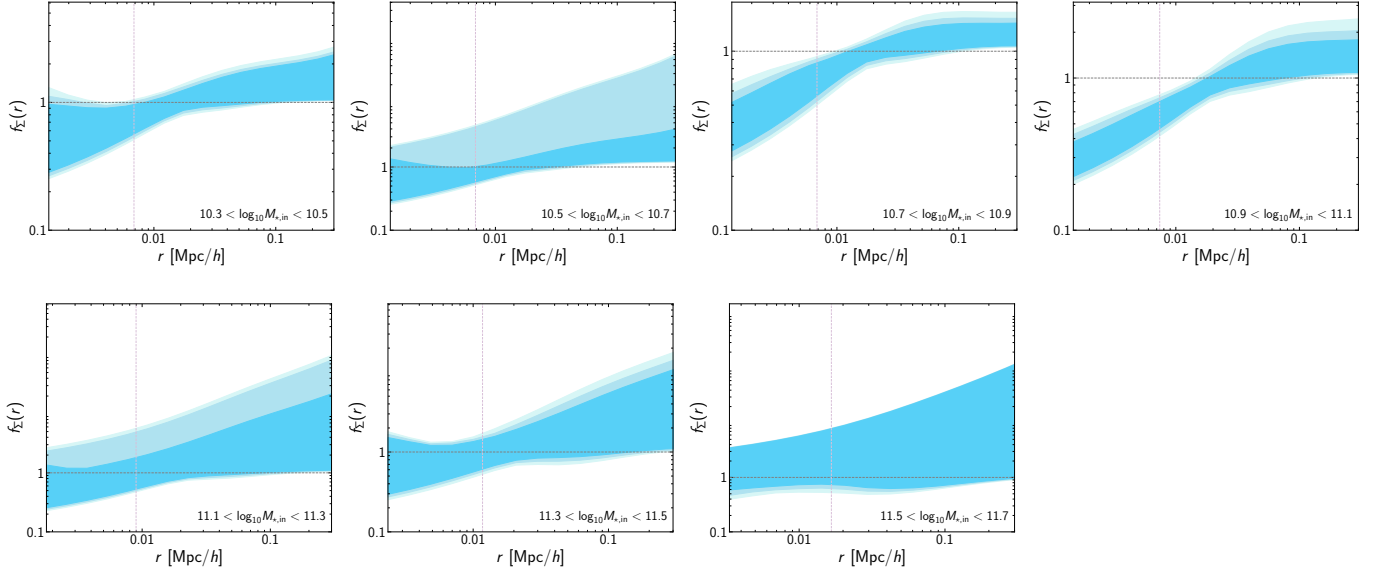


FIG. 5.— The ratio of the surface mass densities $f_{\Sigma}(r)$ defined in Equation (28). The shaded regions represent the 1σ , 2σ , and 3σ confidence intervals from darker to lighter colors. The vertical dashed line shows $r = 5r_e$. Different panels show results for different stellar mass bins.

4. CONCLUSION

We have investigated stellar mass and central dark matter density profiles of photometric LRGs in seven stellar mass bins in the range $10^{10.3}M_{\odot} < M_{*,\text{in}} < 10^{11.7}M_{\odot}$ with the stacked weak gravitational lensing analysis of the Subaru HSC-SSP data. For each stellar mass bin, the inner part of the differential surface mass density profile derived from the weak lensing measurements has been fitted with a two-component model consisting of stellar and dark matter components. For the dark matter component, we have considered a model that has a central core and follows a power-law in the outer region.

We have found that the core radii of dark matter distributions are consistent with zero within 2σ for most stellar mass bins, while non-zero core radii have been detected for two stellar mass bins in the range $10^{10.7}M_{\odot} < M_{*,\text{in}} < 10^{11.1}M_{\odot}$. We have also compared the dark matter profiles constrained from fitting of inner lensing profiles with the extrapolation from fitting of outer lensing profiles to an NFW profile. We have found that they agree within $\sim 2\sigma$ for all stellar mass bins except the two stellar mass bins for which non-zero core radii are preferred.

A possible origin of such cores in dark matter distributions for a particular range of stellar masses is the

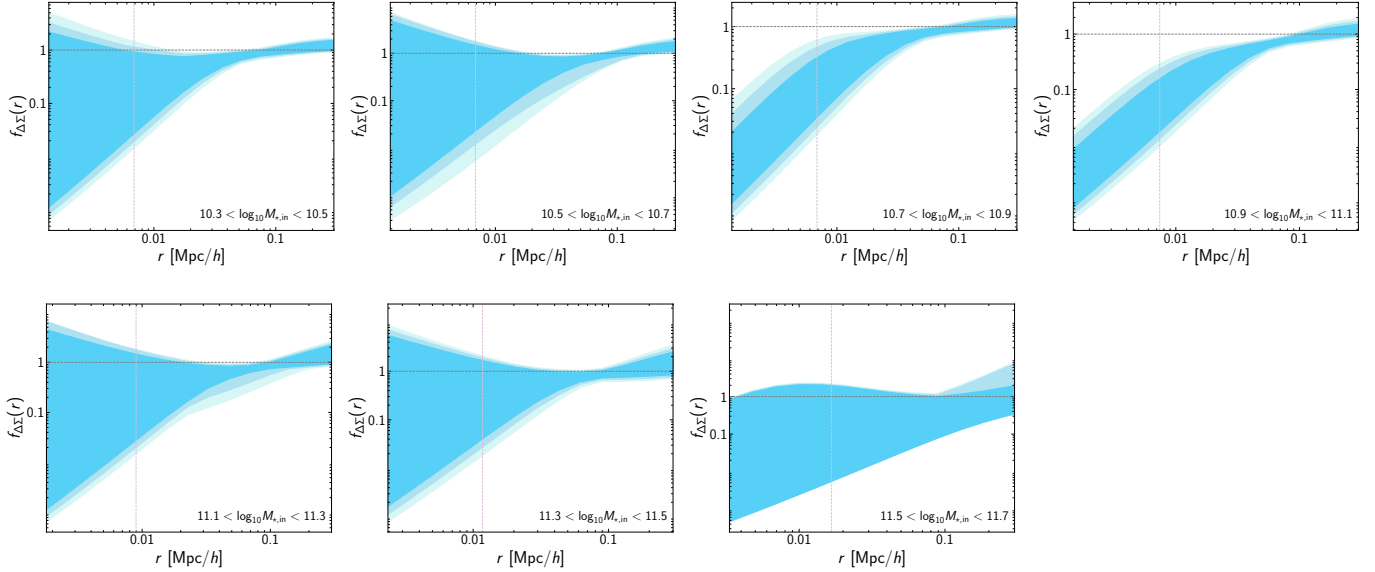


FIG. 6.— Same as Figure 5, but for $f_{\Delta\Sigma}(r)$ defined in Equation (29).

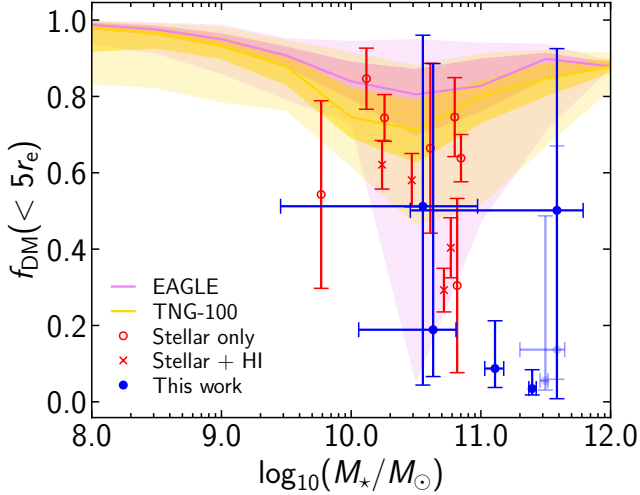


FIG. 7.— Dark matter fractions $f_{DM}(< 5r_e)$. The blue points show our results, while the red points represent the results obtained from the orbit-based dynamical models (Yang et al. 2024). For comparison, solid violet and gold curves show the predictions of the EAGLES and TNG-100 simulations, respectively, with dark and light shaded regions show 1σ and 3σ uncertainties, respectively.

baryonic feedback, as suggested by hydrodynamical simulations. To quantify this feedback effect, we have examined the dark matter fraction within $5r_e$ to find that, for the two stellar mass bins exhibiting cores, the observed dark matter fractions are lower than those predicted by the EAGLES and TNG-100 simulations. Our result is broadly consistent with previous measurements of dark matter fractions with stellar dynamics, and suggests that the actual feedback effect may be stronger than that predicted by the simulations.

Furthermore, we provide a new constraint on the SHMR, where both stellar and halo masses are for the first time directly constrained by weak gravitational lensing. Our results indicate relatively high stellar masses for a given halo mass, and prefer the stellar IMF that is more bottom-heavy than the Salpeter IMF.

Our results have demonstrated that stacked weak lens-

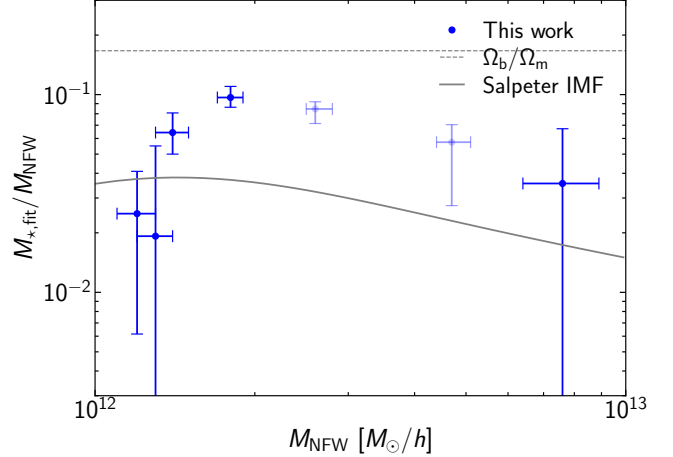


FIG. 8.— The constraint on the SHMR. The vertical and horizontal axes indicate the stellar mass $M_{*,fit}$ obtained from the inner profile fitting normalized by the halo-mass M_{NFW} obtained from the outer profile fitting and M_{NFW} , respectively. The blue points represent our results and the solid line shows the case assuming the Salpeter IMF (Behroozi et al. 2019; Abe et al. 2025). A horizontal dotted line shows Ω_b/Ω_m .

ing is a viable tool to study central density profiles of galaxies and already shed new light on central dark matter profiles, the galaxy-halo connection, and the stellar IMF. In addition to applying the methodology developed in this paper to future galaxy survey data, it is important to extend our work by e.g., considering more flexible dark and stellar mass profiles, studying the redshift dependence, investigating in more detail how the results depend on the choice of the fitting range, and exploring the possible effect of the scatter of density profiles among different galaxies, which deserve further exploration in future work. Furthermore, combining weak lensing constraints with those from strong gravitational lensing and stellar dynamics measurements will lead to even tighter constraints on the central dark matter distribution.

ACKNOWLEDGMENTS

We thank Meng Yang for kindly sharing the numerical data that are used in Figure 7. This work was supported by JSPS KAKENHI Grant Numbers JP25H00662, JP25H00672.

The Hyper Suprime-Cam (HSC) collaboration includes the astronomical communities of Japan and Taiwan, and Princeton University. The HSC instrumentation and software were developed by the National Astronomical Observatory of Japan (NAOJ), the Kavli Institute for the Physics and Mathematics of the Universe (Kavli IPMU), the University of Tokyo, the High Energy Accelerator Research Organization (KEK), the Academia Sinica Institute for Astronomy and Astrophysics in Taiwan (ASIAA), and Princeton University. Funding was contributed by the FIRST program from the Japanese Cabinet Office, the Ministry of Education, Culture, Sports, Science and Technology (MEXT), the Japan Society for the Promotion of Science (JSPS), Japan Science and Technology Agency (JST), the Toray Science Foundation, NAOJ, Kavli IPMU, KEK, ASIAA, and Princeton University.

This paper is based on data collected at the Subaru Telescope and retrieved from the HSC data archive system, which is operated by Subaru Telescope and Astronomy Data Center (ADC) at NAOJ. Data analysis was in part carried out with the cooperation of Center for Computational Astrophysics (CfCA) at NAOJ. We are

honored and grateful for the opportunity of observing the Universe from Maunakea, which has the cultural, historical and natural significance in Hawaii.

This paper makes use of software developed for Vera C. Rubin Observatory. We thank the Rubin Observatory for making their code available as free software at <http://pipelines.lsst.io/>.

The Pan-STARRS1 Surveys (PS1) and the PS1 public science archive have been made possible through contributions by the Institute for Astronomy, the University of Hawaii, the Pan-STARRS Project Office, the Max Planck Society and its participating institutes, the Max Planck Institute for Astronomy, Heidelberg, and the Max Planck Institute for Extraterrestrial Physics, Garching, The Johns Hopkins University, Durham University, the University of Edinburgh, the Queen's University Belfast, the Harvard-Smithsonian Center for Astrophysics, the Las Cumbres Observatory Global Telescope Network Incorporated, the National Central University of Taiwan, the Space Telescope Science Institute, the National Aeronautics and Space Administration under grant No. NNX08AR22G issued through the Planetary Science Division of the NASA Science Mission Directorate, the National Science Foundation grant No. AST-1238877, the University of Maryland, Eotvos Lorand University (ELTE), the Los Alamos National Laboratory, and the Gordon and Betty Moore Foundation.

REFERENCES

- Abe, K. T., Oguri, M., Birrer, S., et al. 2025, *The Open Journal of Astrophysics*, 8, 8, doi: [10.33232/001c.128482](https://doi.org/10.33232/001c.128482)
- Aguado, D. S., Ahumada, R., Almeida, A., et al. 2019, *ApJS*, 240, 23, doi: [10.3847/1538-4365/aaf651](https://doi.org/10.3847/1538-4365/aaf651)
- Aihara, H., Arimoto, N., Armstrong, R., et al. 2018, *PASJ*, 70, S4, doi: [10.1093/pasj/psx066](https://doi.org/10.1093/pasj/psx066)
- Alabi, A. B., Forbes, D. A., Romanowsky, A. J., et al. 2017, *MNRAS*, 468, 3949, doi: [10.1093/mnras/stx678](https://doi.org/10.1093/mnras/stx678)
- Auger, M. W., Treu, T., Gavazzi, R., et al. 2010, *ApJ*, 721, L163, doi: [10.1088/2041-8205/721/2/L163](https://doi.org/10.1088/2041-8205/721/2/L163)
- Baltz, E. A., Marshall, P., & Oguri, M. 2009, *J. Cosmology Astropart. Phys.*, 2009, 015, doi: [10.1088/1475-7516/2009/01/015](https://doi.org/10.1088/1475-7516/2009/01/015)
- Barnabè, M., Czoske, O., Koopmans, L. V. E., Treu, T., & Bolton, A. S. 2011, *MNRAS*, 415, 2215, doi: [10.1111/j.1365-2966.2011.18842.x](https://doi.org/10.1111/j.1365-2966.2011.18842.x)
- Behroozi, P., Wechsler, R. H., Hearin, A. P., & Conroy, C. 2019, *MNRAS*, 488, 3143, doi: [10.1093/mnras/stz1182](https://doi.org/10.1093/mnras/stz1182)
- Bolton, A. S., Brownstein, J. R., Kochanek, C. S., et al. 2012, *ApJ*, 757, 82, doi: [10.1088/0004-637X/757/1/82](https://doi.org/10.1088/0004-637X/757/1/82)
- Bruzual, G., & Charlot, S. 2003, *MNRAS*, 344, 1000, doi: [10.1046/j.1365-8711.2003.06897.x](https://doi.org/10.1046/j.1365-8711.2003.06897.x)
- Bullock, J. S., & Boylan-Kolchin, M. 2017, *ARA&A*, 55, 343, doi: [10.1146/annurev-astro-091916-055313](https://doi.org/10.1146/annurev-astro-091916-055313)
- Cappellari, M. 2016, *ARA&A*, 54, 597, doi: [10.1146/annurev-astro-082214-122432](https://doi.org/10.1146/annurev-astro-082214-122432)
- Cappellari, M., McDermid, R. M., Alatalo, K., et al. 2012, *Nature*, 484, 485, doi: [10.1038/nature10972](https://doi.org/10.1038/nature10972)
- Cappellari, M., Scott, N., Alatalo, K., et al. 2013, *MNRAS*, 432, 1709, doi: [10.1093/mnras/stt562](https://doi.org/10.1093/mnras/stt562)
- Crain, R. A., Schaye, J., Bower, R. G., et al. 2015, *MNRAS*, 450, 1937, doi: [10.1093/mnras/stv725](https://doi.org/10.1093/mnras/stv725)
- DESI Collaboration, Abdul-Karim, M., Adame, A. G., et al. 2025, *arXiv e-prints*, [arXiv:2503.14745](https://arxiv.org/abs/2503.14745), doi: [10.48550/arXiv.2503.14745](https://doi.org/10.48550/arXiv.2503.14745)
- Diemer, B. 2018, *ApJS*, 239, 35, doi: [10.3847/1538-4365/aace8c](https://doi.org/10.3847/1538-4365/aace8c)
- Diemer, B., & Joyce, M. 2019, *ApJ*, 871, 168, doi: [10.3847/1538-4357/aafad6](https://doi.org/10.3847/1538-4357/aafad6)
- Diemer, B., & Kravtsov, A. V. 2015, *ApJ*, 799, 108, doi: [10.1088/0004-637X/799/1/108](https://doi.org/10.1088/0004-637X/799/1/108)
- Ding, Y., Zhu, L., van de Ven, G., et al. 2023, *A&A*, 672, A84, doi: [10.1051/0004-6361/202244558](https://doi.org/10.1051/0004-6361/202244558)
- Etherington, A., Nightingale, J. W., Massey, R., et al. 2023, *MNRAS*, 521, 6005, doi: [10.1093/mnras/stad582](https://doi.org/10.1093/mnras/stad582)
- Gavazzi, R., Treu, T., Rhodes, J. D., et al. 2007, *ApJ*, 667, 176, doi: [10.1086/519237](https://doi.org/10.1086/519237)
- Gnedin, O. Y., Kravtsov, A. V., Klypin, A. A., & Nagai, D. 2004, *ApJ*, 616, 16, doi: [10.1086/424914](https://doi.org/10.1086/424914)
- Grillo, C. 2012, *ApJ*, 747, L15, doi: [10.1088/2041-8205/747/1/L15](https://doi.org/10.1088/2041-8205/747/1/L15)
- Hayashi, K., Kaneda, Y., Mori, M., & Shinozaki, M. 2025, *arXiv e-prints*, [arXiv:2507.22155](https://arxiv.org/abs/2507.22155), doi: [10.48550/arXiv.2507.22155](https://doi.org/10.48550/arXiv.2507.22155)
- Hernández-Martín, B., Schrabback, T., Hoekstra, H., et al. 2020, *A&A*, 640, A117, doi: [10.1051/0004-6361/202037844](https://doi.org/10.1051/0004-6361/202037844)
- Hernquist, L. 1990, *ApJ*, 356, 359, doi: [10.1086/168845](https://doi.org/10.1086/168845)
- Hoekstra, H. 2003, *MNRAS*, 339, 1155, doi: [10.1046/j.1365-8711.2003.06264.x](https://doi.org/10.1046/j.1365-8711.2003.06264.x)
- Huang, S., Leauthaud, A., Greene, J. E., et al. 2018, *MNRAS*, 475, 3348, doi: [10.1093/mnras/stx3200](https://doi.org/10.1093/mnras/stx3200)
- Ishikawa, S., Okumura, T., Oguri, M., & Lin, S.-C. 2021, *ApJ*, 922, 23, doi: [10.3847/1538-4357/ac1f90](https://doi.org/10.3847/1538-4357/ac1f90)
- Keeton, C. R. 2001, *arXiv e-prints*, astro, doi: [10.48550/arXiv.astro-ph/0102341](https://doi.org/10.48550/arXiv.astro-ph/0102341)
- Khadka, N., Birrer, S., Leauthaud, A., & Nix, H. 2024, *MNRAS*, 533, 795, doi: [10.1093/mnras/stae1832](https://doi.org/10.1093/mnras/stae1832)
- Kobayashi, M. I. N., Leauthaud, A., More, S., et al. 2015, *MNRAS*, 449, 2128, doi: [10.1093/mnras/stv424](https://doi.org/10.1093/mnras/stv424)
- Koopmans, L. V. E., Treu, T., Bolton, A. S., Burles, S., & Moustakas, L. A. 2006, *ApJ*, 649, 599, doi: [10.1086/505696](https://doi.org/10.1086/505696)
- Li, R., Shu, Y., & Wang, J. 2018, *MNRAS*, 480, 431, doi: [10.1093/mnras/sty1813](https://doi.org/10.1093/mnras/sty1813)
- Li, X., Miyatake, H., Luo, W., et al. 2022, *PASJ*, 74, 421, doi: [10.1093/pasj/psac006](https://doi.org/10.1093/pasj/psac006)
- Mandelbaum, R., Miyatake, H., Hamana, T., et al. 2018, *PASJ*, 70, S25, doi: [10.1093/pasj/psx130](https://doi.org/10.1093/pasj/psx130)
- Marinacci, F., Vogelsberger, M., Pakmor, R., et al. 2018, *MNRAS*, 480, 5113, doi: [10.1093/mnras/sty2206](https://doi.org/10.1093/mnras/sty2206)
- Medezinski, E., Oguri, M., Nishizawa, A. J., et al. 2018, *PASJ*, 70, 30, doi: [10.1093/pasj/psy009](https://doi.org/10.1093/pasj/psy009)
- Naiman, J. P., Pillepich, A., Springel, V., et al. 2018, *MNRAS*, 477, 1206, doi: [10.1093/mnras/sty618](https://doi.org/10.1093/mnras/sty618)

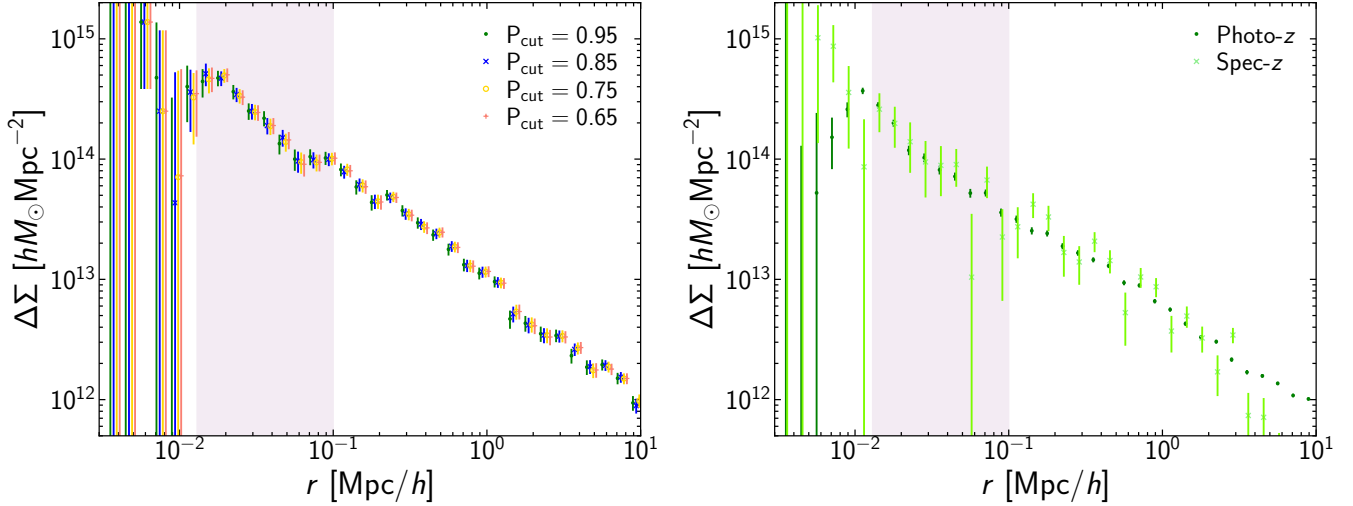


FIG. 9.— *Left:* Dependence of lensing profiles on variations in P_{cut} for the stellar mass bin of $10^{11.5} M_{\odot} < M_{*,\text{in}} < 10^{11.7} M_{\odot}$. *Right:* Comparison between the results obtained using photometric and spectroscopic redshifts of LRGs for the stellar mass bin of $10^{10.9} M_{\odot} < M_{*,\text{in}} < 10^{11.1} M_{\odot}$. In both left and right panels, some points are shifted horizontally for illustrative purpose.

Navarro, J. F., Frenk, C. S., & White, S. D. M. 1997, *ApJ*, 490, 493, doi: [10.1086/304888](https://doi.org/10.1086/304888)
 Nelson, D., Pillepich, A., Springel, V., et al. 2018, *MNRAS*, 475, 624, doi: [10.1093/mnras/stx3040](https://doi.org/10.1093/mnras/stx3040)
 Newman, A. B., Ellis, R. S., & Treu, T. 2015, *ApJ*, 814, 26, doi: [10.1088/0004-637X/814/1/26](https://doi.org/10.1088/0004-637X/814/1/26)
 Oguri, M. 2014, *MNRAS*, 444, 147, doi: [10.1093/mnras/stu1446](https://doi.org/10.1093/mnras/stu1446)
 Oguri, M., & Hamana, T. 2011, *MNRAS*, 414, 1851, doi: [10.1111/j.1365-2966.2011.18481.x](https://doi.org/10.1111/j.1365-2966.2011.18481.x)
 Oguri, M., Rusu, C. E., & Falco, E. E. 2014, *MNRAS*, 439, 2494, doi: [10.1093/mnras/stu106](https://doi.org/10.1093/mnras/stu106)
 Oguri, M., Lin, Y.-T., Lin, S.-C., et al. 2018a, *PASJ*, 70, S20, doi: [10.1093/pasj/psx042](https://doi.org/10.1093/pasj/psx042)
 Oguri, M., Miyazaki, S., Hikage, C., et al. 2018b, *PASJ*, 70, S26, doi: [10.1093/pasj/psx070](https://doi.org/10.1093/pasj/psx070)
 Oguri, M., Lin, Y.-T., Okabe, N., et al. 2025, *PASJ*, submitted
 Oh, S.-H., Hunter, D. A., Brinks, E., et al. 2015, *AJ*, 149, 180, doi: [10.1088/0004-6256/149/6/180](https://doi.org/10.1088/0004-6256/149/6/180)
 Okabe, N., & Smith, G. P. 2016, *MNRAS*, 461, 3794, doi: [10.1093/mnras/stw1539](https://doi.org/10.1093/mnras/stw1539)
 Oldham, L. J., & Auger, M. W. 2018, *MNRAS*, 476, 133, doi: [10.1093/mnras/sty065](https://doi.org/10.1093/mnras/sty065)
 Pillepich, A., Nelson, D., Hernquist, L., et al. 2018, *MNRAS*, 475, 648, doi: [10.1093/mnras/stx3112](https://doi.org/10.1093/mnras/stx3112)
 Rusin, D., Kochanek, C. S., & Keeton, C. R. 2003, *ApJ*, 595, 29, doi: [10.1086/377356](https://doi.org/10.1086/377356)
 Salpeter, E. E. 1955, *ApJ*, 121, 161, doi: [10.1086/145971](https://doi.org/10.1086/145971)
 Santucci, G., Brough, S., van de Sande, J., et al. 2022, *ApJ*, 930, 153, doi: [10.3847/1538-4357/ac5bd5](https://doi.org/10.3847/1538-4357/ac5bd5)
 Schaye, J., Crain, R. A., Bower, R. G., et al. 2015, *MNRAS*, 446, 521, doi: [10.1093/mnras/stu2058](https://doi.org/10.1093/mnras/stu2058)
 Schechter, P. L., Pooley, D., Blackburne, J. A., & Wambsganss, J. 2014, *ApJ*, 793, 96, doi: [10.1088/0004-637X/793/2/96](https://doi.org/10.1088/0004-637X/793/2/96)

Shajib, A. J., Treu, T., Birrer, S., & Sonnenfeld, A. 2021, *MNRAS*, 503, 2380, doi: [10.1093/mnras/stab536](https://doi.org/10.1093/mnras/stab536)
 Sheu, W., Shajib, A. J., Treu, T., et al. 2025, *MNRAS*, 541, 1, doi: [10.1093/mnras/staf976](https://doi.org/10.1093/mnras/staf976)
 Sonnenfeld, A. 2025, *A&A*, 697, A95, doi: [10.1051/0004-6361/202452846](https://doi.org/10.1051/0004-6361/202452846)
 Sonnenfeld, A., Jaelani, A. T., Chan, J., et al. 2019, *A&A*, 630, A71, doi: [10.1051/0004-6361/201935743](https://doi.org/10.1051/0004-6361/201935743)
 Sonnenfeld, A., Leauthaud, A., Auger, M. W., et al. 2018, *MNRAS*, 481, 164, doi: [10.1093/mnras/sty2262](https://doi.org/10.1093/mnras/sty2262)
 Sonnenfeld, A., Treu, T., Gavazzi, R., et al. 2013, *ApJ*, 777, 98, doi: [10.1088/0004-637X/777/2/98](https://doi.org/10.1088/0004-637X/777/2/98)
 Sonnenfeld, A., Treu, T., Marshall, P. J., et al. 2015, *ApJ*, 800, 94, doi: [10.1088/0004-637X/800/2/94](https://doi.org/10.1088/0004-637X/800/2/94)
 Springel, V., Pakmor, R., Pillepich, A., et al. 2018, *MNRAS*, 475, 676, doi: [10.1093/mnras/stx3304](https://doi.org/10.1093/mnras/stx3304)
 Tinker, J. L., Robertson, B. E., Kravtsov, A. V., et al. 2010, *ApJ*, 724, 878, doi: [10.1088/0004-637X/724/2/878](https://doi.org/10.1088/0004-637X/724/2/878)
 Treu, T., Auger, M. W., Koopmans, L. V. E., et al. 2010, *ApJ*, 709, 1195, doi: [10.1088/0004-637X/709/2/1195](https://doi.org/10.1088/0004-637X/709/2/1195)
 Treu, T., & Koopmans, L. V. E. 2004, *ApJ*, 611, 739, doi: [10.1086/422245](https://doi.org/10.1086/422245)
 van der Wel, A., Martorano, M., Häußler, B., et al. 2024, *ApJ*, 960, 53, doi: [10.3847/1538-4357/ad02ee](https://doi.org/10.3847/1538-4357/ad02ee)
 van Dokkum, P. G., & Conroy, C. 2010, *Nature*, 468, 940, doi: [10.1038/nature09578](https://doi.org/10.1038/nature09578)
 Yang, M., Zhu, L., Lei, Y., et al. 2024, *MNRAS*, 528, 5295, doi: [10.1093/mnras/stae335](https://doi.org/10.1093/mnras/stae335)
 Zhu, K., Lu, S., Cappellari, M., et al. 2024, *MNRAS*, 527, 706, doi: [10.1093/mnras/stad3213](https://doi.org/10.1093/mnras/stad3213)

APPENDIX

TESTS OF SYSTEMATICS IN WEAK LENSING MEASUREMENTS

Background galaxy selection

We check the validity of our choice of the value of P_{cut} in Equation (7) by checking how measured lensing profiles are affected by the value of P_{cut} . The result for the stellar mass bin of $10^{11.5} M_{\odot} < M_{*,\text{in}} < 10^{11.7} M_{\odot}$, which corresponds to the highest stellar mass bin and therefore is expected to be most significantly affected by the dilution effect, is shown in the left panel of Figure 9. Since the lensing signal becomes unstable in the range $r \leq 0.013 h^{-1} \text{Mpc}$, we exclude that from the fitting range. We have confirmed that, for the other stellar mass bins, the results are also stable against variations in P_{cut} in the range $r > 0.013 h^{-1} \text{Mpc}$.

Effect of the photometric redshift uncertainty of LRGs

To examine the impact of the photometric redshift uncertainty of photometric LRGs, we compare our results with those using LRGs with spectroscopic redshifts. To do so, we first cross match the photometric LRGs with a compilation of spectroscopic galaxies constructed in [Oguri et al. \(2025\)](#), which is used to calibrate the stellar population synthesis model in the CAMIRA algorithm. The majority of the spectroscopic galaxies at $0.4 < z < 0.6$ are those from the SDSS ([Aguado et al. 2019](#)) and DESI ([DESI Collaboration et al. 2025](#)). We then rerun the algorithm to select photometric LRGs with redshifts of cross-matched galaxies fixed to the spectroscopic redshifts to re-compute their stellar masses. The number of these spectroscopic LRGs is roughly a factor of 10 smaller than that of the photometric LRGs. The result for the stellar mass bin $10^{10.9}M_{\odot} < M_{\star,\text{in}} < 10^{11.1}M_{\odot}$ is shown in the right panel of Figure 9. Defining the chi-square as

$$\chi^2 = \sum_{i=1}^N \frac{(\Delta\Sigma_{\text{spec},i} - \Delta\Sigma_{\text{photo},i})^2}{\sigma_{\text{spec},i}^2 + \sigma_{\text{photo},i}^2}, \quad (\text{A1})$$

we obtain $\chi^2 \approx 4.6$ within the fitting range for the inner density profile ($N = 9$ bins) for this stellar mass bin. Here, $\Delta\Sigma_{\text{photo}}$, σ_{photo} and $\Delta\Sigma_{\text{spec}}$, σ_{spec} are the differential surface mass densities and their errors derived from the photometric and spectroscopic LRGs, respectively. Since the value of χ^2 lies within the 95% confidence interval ($2.7 \lesssim \chi^2 \lesssim 19.0$), the difference of lensing profiles between the photometric and spectroscopic LRGs is not statistically significant. Therefore, we conclude that the effect of the photometric redshift uncertainty of LRGs is negligible. We have computed χ^2 for other stellar mass bins as well, and for the stellar mass bin $10^{11.3}M_{\odot} < M_{\star,\text{in}} < 10^{11.5}M_{\odot}$, we find that $\chi^2 \approx 22.8$ that falls outside the 95% confidence interval. Therefore, the data in this bin are less reliable and should be interpreted with caution. We find that the values of χ^2 for the other mass bins are well within $2.7 \lesssim \chi^2 \lesssim 19.0$, indicating that the differences of lensing profiles between the photometric and spectroscopic LRGs are also negligible for those stellar mass bins.

Cross shear

The cross shear profile should be consistent with zero in the absence of any systematic errors, and hence is used to check systematic errors in tangential shear profile measurements. We define the chi-square as

$$\chi^2 = \sum_{i=1}^N \frac{\Delta\Sigma_{\times,i}^2}{\sigma_{\times,i}^2}, \quad (\text{A2})$$

where $\Delta\Sigma_{\times}$ and σ_{\times} are the differential surface mass density and its error derived from the cross shear, respectively. For the fitting range for the inner density profile ($N = 9$ bins), we obtain χ^2 ranging from 2.2 to 14.55 across the stellar mass bins, which mostly lie within the 95% confidence interval ($2.7 \lesssim \chi^2 \lesssim 19.0$). Therefore this cross shear test suggests no sign of systematics for the innermost lensing profiles that are our main interest in this study. We also check the χ^2 values for all the fitting range of the inner and outer density profiles ($N = 24$ bins). We obtain χ^2 ranging from 14.9 to 37.4 across the stellar mass bins, which again lie within the 95% confidence interval ($12.4 \lesssim \chi^2 \lesssim 39.4$).